INTERNATIONAL JOURNAL FOR NUMERICAL METHODS IN FLUIDS, VOL. 15, 503–524 (1992)

SPIN-UP IN A SEMICIRCULAR CYLINDER

H. I. ANDERSSON

Division of Applied Mechanics, Department of Mechanical Engineering, The Norwegian Institute of Technology, N-7034 Trondheim, Norway

J. T. BILLDAL

SINTEF Fluid Machinery, N-7034 Trondheim, Norway

AND

G. J. F. VAN HEIJST

Fluid Dynamics Laboratory, Department of Physics, Eindhoven University of Technology, P.O. Box 513, NL-5600 MB Eindhoven, The Netherlands

SUMMARY

This paper addresses the spin-up from rest of a free-surface fluid confined in a cylindrical container with a semicircular cross-section. The flow in the various stages of the spin-up process has been calculated numerically by using the finite-volume technique on a three-dimensional grid. Local grid refinement was applied in order to capture the effects of the boundary layer at the lateral boundaries and of the Ekman layer at the bottom. The numerical results agree very well with laboratory observations.

KEY WORDS Spin-up Viscous flow Time-dependent Ekman layers Finite volume Fractional step

1. INTRODUCTION

The spin-up of a homogeneous fluid in a container, either from rest or from a state of slower solid-body rotation, is a fundamental problem in fluid mechanics. The problem, apart from being interesting from the pure scientific point of view, has many applications ranging from engineering to geophysical situations. Most previous studies concerned the spin-up of fluid contained in an axisymmetric tank, and a review of earlier works on this problem is given by Benton and Clark.[1]

It was pointed out by Greenspan and Howard[2] that the Ekman layers at the horizontal boundaries of the flow domain play a crucial role in the spin-up process in generating a secondary circulation in the meridional plane. In a thorough analysis of the linear case, i.e. the spin-up from an initial state of solid-body rotation at angular speed Ω to an ultimate state of solid-body rotation at speed $\Omega + \Delta\Omega$ (with $\Delta\Omega \ll \Omega$), they derived the timescale of the adjustment process to be $T_E \approx E^{-1/2} \cdot T \approx H/(\nu\Omega)^{1/2}$, with $T = 2\pi/\Omega$ the rotation period, H the height of the closed container, ν the kinematic viscosity, and $E = \nu/\Omega H^2$ the Ekman number. In later studies it was found that this timescale also applies to the non-linear case ($\Delta\Omega \sim \Omega$). Although this type of spin-up is already rather complicated, the presence of a density stratification further complicates the adjustment process to a considerable degree.[3–7]

Recently it was demonstrated in experimental studies by van Heijst[8] and by van Heijst *et al.*[9] that the spin-up process in non-axisymmetric containers displays some new features not observed in the axisymmetric cases. The authors considered a number of different container geometries

0271–2091/92/170503–22$16.00

Received July 1991
Revised February 1992

(annular tank with a radial barrier, semicircular tank, square tank), and it was found that the adjustment to the ultimate solid-body rotation was characterized by three principal stages, namely (i) the zero-vorticity starting flow, followed by (ii) flow separation from the lateral tank walls, leading to irregular flows, soon followed by (iii) organization of the flow into a regular cell pattern. Once this cellular pattern is established, the flow becomes quasi-stationary, and gradually decays due to the Ekman layers at the horizontal boundaries, until the ultimate state of rigid-body rotation is reached. This phenomenon of 'self-organization' into a number of cells is attributed to the two-dimensional (2D) nature of the rotating flow. Apart from the starting flow (which can be described in terms of potential theory), the flow in the subsequent stages is rather complicated, and does not allow a straightforward analytical description.

In order to obtain a deeper insight into the flow during the various stages of the spin-up process, it was therefore decided to perform a numerical simulation of the unsteady flow by integrating the incompressible Navier–Stokes equations in time. This is not a simple task, since three-dimensional (3D) effects (the presence of the Ekman layer at the bottom) play a crucial role in the adjustment process. However, the finite-volume concept of Billdal and Andersson[10] for unsteady viscous flow problems, which recently proved successful in predicting time-dependent flows in rotating and non-rotating 2D configurations, can undoubtedly be generalized to 3D situations. In this paper the numerical results of a time-dependent 3D simulation of the spin-up are compared with laboratory observations for one particular case, viz. that of the semicircular tank described by van Heijst.[8] In order to facilitate this comparison and enhance the understanding of the flow phenomena, the sequence of streakline photographs in Reference 8 is supplemented by streakline patterns at intermediate time levels. Moreover, a quantitative comparison is made possible through the new data for the time-varying position of the separation point at the plane wall.

The experimental arrangement consists of a cylindrical tank (inner diameter 92.5 cm, working height 35 cm), placed concentrically on a turntable. The angular speed Ω of the turntable is adjustable in the range of 0–2 rad s^{-1}. The tank is filled with a homogeneous fluid with density ρ and kinematic viscosity ν. A solid wall is placed along a diameter, so that the tank is divided into two areas of semicircular cross-sections. Hereafter, attention is focused on only one of these flow domains. Initially ($t<0$), $\Omega=0$ and the fluid is completely at rest, with a uniform depth H. At $t=0$ the table starts rotating, and its angular speed is quickly brought to some fixed value $\Omega>0$. The resulting flow is visualized by small tracer particles floating on the free surface of the fluid. A photo camera is mounted in the rotating frame, at some distance above the free surface. The streak photographs obtained with a prescribed exposure time τ allow accurate measurement of the velocity field at the upper surface, which is assumed to be representative of the flow at lower levels (but outside the bottom Ekman layer).

The adjustment of the flow to the ultimate state of solid-body rotation at speed Ω is characterized by a number of stages, which were first described by van Heijst[8]: immediately after the start of the experiment the relative flow has the appearance of a large cell of retrograde (anticyclonic) motion, filling the domain completely. Soon thereafter, flow separation is observed to occur at the downstream ends of the flat and the curved lateral boundaries of the flow domain. This flow separation results in the formation of cyclonic flow cells, which are seen to merge in the next stages, largely destroying the original anticyclonic cell. Eventually, a more or less steady two-cell pattern is established, consisting of a cyclonic and an anticyclonic cell. This relative motion gradually decays as a result of the 'ordinary' spin-up/spin-down mechanism provided by the Ekman layer at the bottom of the container.

In the present paper the results of the time-dependent 3D numerical simulation of this spin-up flow is compared with the laboratory observations. Along with a qualitative comparison of the

subsequent flow patterns, a more quantitative comparison is made as well, viz. by considering the time-dependent position of the separation point at the flat wall. In addition, the numerical simulation provides information about the secondary meridional flow, the bottom Ekman layer, and the changing spatial vorticity distribution of the flow field; this information is not readily available in the laboratory, but is nevertheless important in order to obtain a better understanding of the flow evolution.

The sequel of the paper is organized as follows: the mathematical problem is formulated in Section 2, followed by a description of the numerical techniques in Section 3. The numerical results are presented in Section 4, and a comparison is made with the laboratory experiments. Finally, some conclusions are given in Section 5.

2. MATHEMATICAL MODELLING

2.1. Governing equations

Unsteady motion of a viscous fluid obeys the time-dependent Navier–Stokes equations. The governing equations in primitive variables for the flow of an incompressible fluid with constant density in a rotating frame of reference are the mass continuity

$$\frac{\partial u_i}{\partial x_i}=0 \tag{1}$$

and the momentum equation

$$\rho\frac{\partial u_i}{\partial t}+\frac{\partial}{\partial x_j}\left[\rho u_i u_j+p\delta_{ij}-\mu\left(\frac{\partial u_i}{\partial x_j}+\frac{\partial u_j}{\partial x_i}\right)\right]=-\rho\varepsilon_{ijk}\Omega_j[2u_k+\varepsilon_{klm}\Omega_l r_m] \tag{2}$$

where p is the pressure and u_i denotes the velocity component in the x_i-direction in a Cartesian co-ordinate system. Here, Ω is the constant angular velocity of the reference frame, $\mathbf{r}$ is the position vector in the rotating frame, ρ is the density and μ is the viscosity of the fluid, while δ_{ij} and ε_{ijk} are the Kronecker delta and Levi–Civita symbols, respectively. The convective terms on the left-hand side of equation (2) are intentionally expressed in conservative form. The terms on the right-hand side, which arise only in rotating co-ordinate systems, represent the fictitious Coriolis and centrifugal forces per unit volume.

2.2. Boundary conditions

The specification of the problem is completed by the boundary conditions

$$u_i=0 \tag{3}$$

at a solid wall, and

$$u_i N_i=0 \tag{4}$$

at a passive free surface of the fluid. Here, equation (3) is the standard no-slip condition for viscous flow past a solid surface. The more relaxed condition (4), in which N_i denotes a component of the unit vector normal to the boundary Γ, allows the fluid to slip past the free surface but not to penetrate into it. The latter condition is routinely used in numerical analyses of inviscid flow phenomena.

Assuming that elevations and depressions of the free surface are small compared with the total fluid depth H, the topographical surface is approximated by a fictitious horizontal flat

surface. The slip-flow condition (4) is then imposed along this artificial boundary, while the pressure is treated as an unknown variable. The resulting pressure variation along the boundary is believed to mimic the real topography of the free surface, i.e. high-pressure regions are associated with surface elevations while low-pressure zones correspond to depressions of the free surface. This approach is analogous with the 'rigid lid' approximation, which has been successfully used by Rastogi and Rodi[11] and Leschziner and Rodi[12] in their numerical predictions of open-channel flows.

The semicircular flow domain considered in this paper is most conveniently described in terms of cylindrical polar coordinates (r, θ, z), with r measured from the (rotation) axis of the system. The fluid domain is then defined by $0 \leqslant r \leqslant R$; $0 \leqslant \theta \leqslant \pi$; $0 \leqslant z \leqslant H$. The boundary condition (3) thus applies to the bottom $\{0 \leqslant r \leqslant R;\ 0 \leqslant \theta \leqslant \pi;\ z = 0\}$ and to the side walls $\{0 \leqslant r \leqslant R;\ \theta = 0, \pi;\ 0 \leqslant z \leqslant H\}$ and $\{r = R;\ 0 \leqslant \theta \leqslant \pi;\ 0 \leqslant z \leqslant H\}$, whereas the free-surface condition (4) applies to $\{0 \leqslant r \leqslant R;\ 0 \leqslant \theta \leqslant \pi;\ z = H\}$.

3. NUMERICAL METHOD

The finite-volume method has proved successful in predicting steady flows in complex 3D configurations. An approach based on Chorin's artificial compressibility concept[13] has recently been used to solve inviscid[14] as well as viscous[15] and turbulent[16] flow problems. In this approach the steady-state solution is obtained as the ultimate solution of a pseudo-transient calculation, in which the time involved has no physical meaning. Accordingly, the pseudo-time-stepping acts simply as an iterative procedure for the solution of the steady-flow equations.

To carry the attractive features of the finite-volume method over to time-dependent flow problems, a fractional step approach is adopted. The explicit solution of the time-dependent momentum equations is then decoupled from the solution of the mass continuity equation, and an essential part of the algorithm becomes the solution of a Poisson-type equation.

3.1. Finite volume formulation

The integral formulation of the time-dependent, incompressible Navier–Stokes equations (1) and (2) for a small control volume V with surface S becomes

$$\oint_S u_i n_i \, \mathrm{d}S = 0, \tag{5}$$

$$\int_V \frac{\partial u_i}{\partial t} \mathrm{d}V + \oint_S \left[u_i u_j + \frac{p}{\rho} \delta_{ij} - \nu \left(\frac{\partial u_i}{\partial x_j} + \frac{\partial u_j}{\partial x_i} \right) \right] n_j \, \mathrm{d}S = - \int_V \varepsilon_{ijk} \Omega_j [2u_k + \varepsilon_{klm} \Omega_l r_m] \, \mathrm{d}V, \tag{6}$$

where $\nu = \mu/\rho$ is the kinematic viscosity of the fluid and n_i is the component in the x_i-direction of the unit vector normal to the surface S.

3.2. Time integration

The basic principle of the fractional step method, as introduced independently by Chorin[17] and Temam,[18] is that the time evolution is split into intermediate steps. In the explicit version of the method described by Fortin *et al.*,[19] a first-order accurate Euler scheme is used for the discretization in time. Here, this method is adapted to the finite-volume formulation of the governing equations. The time derivative on the left-hand side of the momentum equation (6) is first replaced by an explicit first-order difference approximation. Each time step is subsequently

split into two fractional steps, and the resulting equations for each fractional step can be expressed in semidiscretized form as:

$$\int_V (u_i^* - u_i^m)\,\mathrm{d}V = -\Delta t \oint_S \left[u_i^m u_j^m + \frac{p^m}{\rho}\delta_{ij} - \nu\left(\frac{\partial u_i^m}{\partial x_j} + \frac{\partial u_j^m}{\partial x_i}\right)\right] n_j\,\mathrm{d}S$$

$$-\Delta t \int_V \varepsilon_{ijk}\Omega_j + [2u_k^m + \varepsilon_{klm}\Omega_l r_m]\,\mathrm{d}V \tag{7}$$

$$\int_V (u_i^{m+1} - u_i^*)\,\mathrm{d}V = -\Delta t \oint_S \frac{1}{\rho}(p^{m+1} - p^m)\delta_{ij} n_j\,\mathrm{d}S \tag{8}$$

where the superscripts signify the actual time levels, Δt is the time increment between time levels m and $m+1$, and u_i^* denotes the intermediate, or tentative, velocity field. It should be noticed that u_i^*, which carries the correct vorticity, generally fails to satisfy mass continuity.

An essential feature of the decomposition given by equation (7) and (8), is that the tentative velocity field u_i^* can be calculated explicitly from equation (7), while the new velocity field u_i^{m+1} is related to the new pressure field p^{m+1} by equation (8). Thus, by taking the divergence of equation (8), imposing the continuity constraint (5) at time level $m+1$, and subsequently making use of Gauss divergence theorem, we obtain

$$\frac{1}{\rho}\oint_S \frac{\partial}{\partial x_i}(p^{m+1} - p^m) n_i\,\mathrm{d}S = \frac{1}{\Delta t}\oint_S u_i^* n_i\,\mathrm{d}S. \tag{9}$$

This equation is readily recognized as an integral form of a Poisson equation for the pressure increment $p^{m+1} - p^m$, in which the surface integral on the right-hand side represents the net volume flow due to u_i^* out of V. The resulting solution algorithm, therefore, consists of the following three basic steps:

(i) Solve (7) explicitly for u_i^*,
(ii) Solve (9) for the pressure increment $p^{m+1} - p^m$;
(iii) Evaluate the new velocity field u_i^{m+1} from (8).

3.3. Boundary conditions

Provided that the boundary conditions imposed on the pressure field are consistent with equation (8), the solution for the velocity field u_i^{m+1} turns out to be independent of the boundary conditions imposed on the tentative velocity u_i^* (see e.g. Peyret and Taylor[20]). Therefore, we impose the boundary condition

$$\int_{V'} u_i^* N_i\,\mathrm{d}V = \int_{V'} u_i^{m+1} N_i\,\mathrm{d}V \tag{10}$$

along the entire boundary Γ of the calculation domain, see Figure 1. Here, V' denotes the volume of a cell with surface S', shifted with respect to the computational cells such that the midpoint of V' falls on the boundary of the calculation domain. Equation (8) may then be expressed for the shifted volume V' rather than for V. By projecting this equation on the direction normal to the boundary Γ, i.e. multiplying by the unit vector N_i normal to Γ, the left-hand side of the resulting equation vanishes and we obtain

$$\oint_{S'} (p^{m+1} - p^m) n_i N_i\,\mathrm{d}S = \int_{V'} \frac{\partial}{\partial x_i}(p^{m+1} - p^m) N_i\,\mathrm{d}V = 0 \tag{11}$$

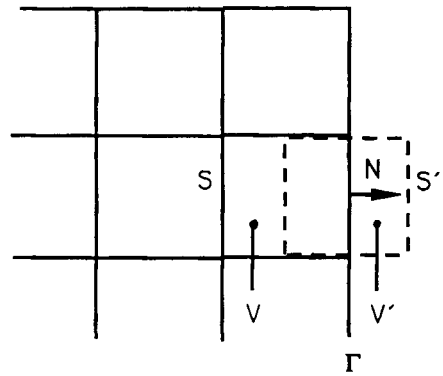

Figure 1. Shifted control volume V' with surface S' (broken lines) at the boundary Γ of the calculation domain

which is readily recognized as an integral form of a Neumann-type boundary condition. It should be emphasized that equation (10) is a condition only on the component of $\mathbf{u}^*$ which is normal to the boundary Γ. According to equations (3) and (4) $u_i N_i$ is supposed to vanish all along the boundary of the calculation domain. The left-hand side of equation (10) should, therefore, be equated to zero at the passive free surface as well as along the solid container walls.

3.4. The Poisson equation for pressure

An essential and time-consuming part of the numerical algorithm is the solution of the Neumann problem defined by the Poisson-like equation (9) subject to the Neumann-type boundary condition (11). In fact, this elliptic problem has to be solved accurately at each time level throughout the calculation. For this purpose a rather simple and yet fairly effective method has been employed, namely, Gauss–Seidel iterations by lines. The resulting tridiagonal matrix is then solved by the Thomas algorithm.

In a recent comparative study[21] of the flow over an impulsively started circular cylinder on a 2D 129×65 computational mesh, the present solution strategy for the Neumann problem proved to be as efficient as a more advanced multigrid solver. This somewhat surprising observation arises because the multigrid cycle cannot be effectively vectorized for the CRAY X-MP vector machine.

3.5. Space discretization

Following a fairly standard approach, the computational domain is divided into a number of hexahedral cells forming the computational mesh. The index system i,j,k is aligned with the curvilinear co-ordinates where i, j, k are indices of the cell in which the flow quantities are updated, see Figure 2. By walking in the positive i-direction, we arrive next at cell $i+1, j, k$, thereby crossing the $i=$constant cell wall which is labeled $i+1/2, j, k$. Applying the cell-centred finite volume discretization technique to the momentum equations (7) on an arbitrary non-orthogonal structured grid, we obtain the following scheme:

$$\mathbf{VOL}_{i,j,k}(\mathbf{v}^*_{i,j,k}-\mathbf{v}^m_{i,j,k})/\Delta t+\mathbf{F}_{i+1/2,j,k}-\mathbf{F}_{i-1/2,j,k}+\mathbf{G}_{i,j+1/2,k}-\mathbf{G}_{i,j-1/2,k}$$
$$+\mathbf{H}_{i,j,k+1/2}-\mathbf{H}_{i,j,k-1/2}=\mathbf{VOL}_{i,j,k}\mathbf{R}_{i,j,k} \tag{12}$$

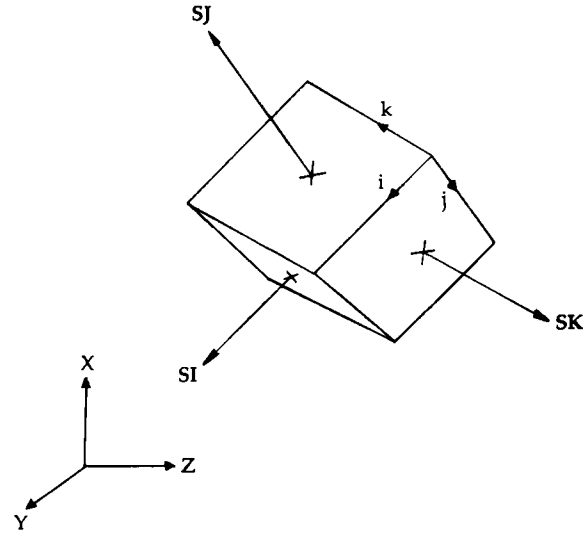

Figure 2. The surface area vectors SI, SJ and SK of a hexahedral cell in the three index directions i, j and k

where $\mathrm{VOL}_{i,j,k}$ is the volume of the grid cell containing the velocity vector $\mathbf{v}_{i,j,k}$ and $\mathbf{F}_{i\pm 1/2,j,k}$, $\mathbf{G}_{i,j\pm 1/2,k}$, $\mathbf{H}_{i,j,k\pm 1/2}$ are the approximated integrated flux of momentum through the six cell walls. The right-hand side vector $\mathbf{R}$ contains lower-order terms due to centrifugal and Coriolis terms in the rotating co-ordinate system.

The inviscid fluxes in the three co-ordinate directions are computed in standard manner,[22,23] i.e. by using averages of the cell-centred values as approximations of wall-centred values. Rizzi and Eriksson[22], for instance, provided explicit expressions for inviscid contributions to the flux vectors $\mathbf{F}$, $\mathbf{G}$ and $\mathbf{H}$. The viscous part, which is of crucial importance in the present study, is calculated by first approximating the gradients of u, v, w at the wall centres and then using these values directly in evaluating the diffusive fluxes. However, for standard definition of the flux terms, i.e.

$$\tau = \nu[\nabla \mathbf{v} + (\nabla \mathbf{v})^{\mathrm{T}}] \tag{13}$$

it is possible to combine these two steps and thereby obtain a simple expression for the integrated flux. For example, the integrated flux of momentum due to viscosity between grid cells i, j, k and $i+1, j, k$ can be approximated by

$$(\tau \cdot \mathbf{SI})_{i+1/2,j,k} = \nu \left\{ \mathrm{VOL}^{-1} \left[|SI|^2 \frac{\partial \mathbf{v}}{\partial i} + (\mathbf{SI} \cdot \mathbf{SJ}) \frac{\partial \mathbf{v}}{\partial j} + (\mathbf{SI} \cdot \mathbf{SK}) \frac{\partial \mathbf{v}}{\partial k} + \left(\mathbf{SI} \cdot \frac{\partial \mathbf{v}}{\partial i} \right) \mathbf{SI} \right. \right.$$
$$\left. \left. + \left(\mathbf{SI} \cdot \frac{\partial \mathbf{v}}{\partial j} \right) \mathbf{SJ} + \left(\mathbf{SI} \cdot \frac{\partial \mathbf{v}}{\partial k} \right) \mathbf{SK} \right] \right\}_{i+1/2,j,k} \tag{14}$$

where all terms are evaluated at $i+1/2, j, k$. The metric term $\mathbf{SI}(i+1/2, j, k)$ is here the standard normal surface area vector ($\mathbf{n}S$) for the cell between grid cell i, j, k and $i+1, j, k$ (see Figure 2) and is, therefore, easily obtained. However, the corresponding normal surface area vector in the j-direction, $\mathbf{SJ}$, is in the standard implementation only defined for integer i, k values and fractional j

values. We are thus forced to construct $\mathbf{SJ}(i+1/2, j, k)$ in a non-standard manner. Here, we choose to approximate it by averaging the four nearest available vectors, i.e.

$$\mathbf{SJ}_{i+1/2,j,k} = 1/4(\mathbf{SJ}_{i,j-1/2,k} + \mathbf{SJ}_{i,j+1/2,k} + \mathbf{SJ}_{i+1,j-1/2,k} + \mathbf{SJ}_{i+1,j+1/2,k}). \tag{15}$$

For the same reason $\mathbf{SK}(i+1/2, j, k)$ is approximated as

$$\mathbf{SK}_{i+1/2,j,k} = 1/4(\mathbf{SK}_{i,j,k-1/2} + \mathbf{SK}_{i,j,k+1/2} + \mathbf{SK}_{i+1,j,k-1/2} + \mathbf{SK}_{i+1,j,k+1/2}). \tag{16}$$

The remaining metric term VOL^{-1} is finally approximated by

$$\mathrm{VOL}^{-1}_{i+1/2,j,k} = 1/2(\mathrm{VOL}^{-1}_{i,j,k} + \mathrm{VOL}^{-1}_{i+1,j,k}). \tag{17}$$

The derivatives of the velocity vector $\mathbf{v} = (u, v, w)$ with respect to the three co-ordinate directions i, j, k are approximated by

$$\begin{aligned}
(\partial \mathbf{v}/\partial i)_{i+1/2,j,k} &= \mathbf{v}_{i+1,j,k} - \mathbf{v}_{i,j,k} \\
(\partial \mathbf{v}/\partial j)_{i+1/2,j,k} &= 1/4(\mathbf{v}_{i,j+1,k} + \mathbf{v}_{i+1,j+1,k} - \mathbf{v}_{i,j-1,k} - \mathbf{v}_{i+1,j-1,k}) \\
(\partial \mathbf{v}/\partial k)_{i+1/2,j,k} &= 1/4(\mathbf{v}_{i,j,k+1} + \mathbf{v}_{i+1,j,k+1} - \mathbf{v}_{i,j,k-1} - \mathbf{v}_{i+1,j,k-1}).
\end{aligned} \tag{18}$$

Equations (12)–(18) constitute a formula by which the viscous momentum flux across an inner constant-i cell wall can be approximated in terms of the standard metric quantities **SI**, **SJ**, **SK** and VOL. Analogous formulas can be written for the fluxes in the **j**- and **k**-direction.

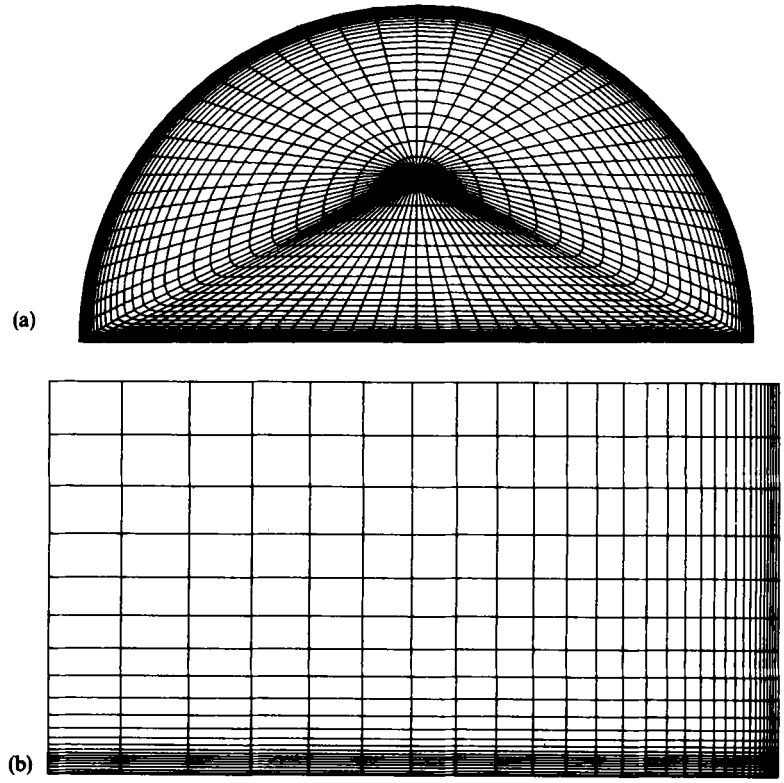

Figure 3. Finite-volume mesh ($79 \times 30 \times 23$ points): (a) top view; (b) side view (vertical midplane)

If $i = 1/2$ is a solid wall, the no-slip boundary conditions are easily obtained by using the fact that $\mathbf{v}$ and the derivatives of $\mathbf{v}$ along the solid wall are zero. Equation (14) will then reduce to

$$(\tau \cdot \mathbf{SI})_{1/2,j,k} = \nu \left\{ \mathrm{VOL}^{-1} \left[|SI|^2 \frac{\partial \mathbf{v}}{\partial i} + \left(\mathbf{SI} \cdot \frac{\partial \mathbf{v}}{\partial i} \right) \mathbf{SI} \right] \right\}_{1/2,j,k}. \tag{19}$$

The gradient of the velocity on the right-hand side is evaluated by one-sided differences. Since the viscous terms are completely centred and the computational molecule is as compact as possible, the discretized form of these terms is consistent with the second-order accuracy obtained for the inviscid flux terms.

The central difference approximations used in this finite-volume scheme give rise to oscillations. Therefore, some numerical damping terms have to be added to the scheme in order to damp the short wavelengths. The total difference operator may accordingly be split into the physical difference operator $\mathbf{S}_{\mathrm{ph}}$, that results from equation (12) by adding the appropriate boundary conditions, and the dissipative part $\mathbf{S}_{\mathrm{n}}(\mathbf{v})$. The scheme of the momentum can now be written as:[22]

$$\mathrm{VOL}_{i,j,k}(\mathbf{v}^*_{i,j,k} - \mathbf{v}^m_{i,j,k}) = \mathbf{S}_{\mathrm{ph}}(\mathbf{v})_{i,j,k} + \mathbf{S}_{\mathrm{n}}(\mathbf{v})_{i,j,k}. \tag{20}$$

In the interior cells of the computational domain, the numerical damping operator is defined by a fourth-order central-difference operator:[22]

$$\mathbf{S}_{\mathrm{n}}(\mathbf{v})_{i,j,k} = -e_4(\delta_i^4 + \delta_j^4 + \delta_k^4)\mathbf{v}_{i,j,k}, \tag{21}$$

where

$$\delta_i \mathbf{v}_{i,j,k} = \mathbf{v}_{i+1/2,j,k} - \mathbf{v}_{i-1/2,j,k}.$$

Equivalent operators are adapted for $\delta_j \mathbf{v}_{i,j,k}$ and $\delta_k \mathbf{v}_{i,j,k}$. As can be seen here, the smoothing operator in 3D is treated as the sum of three 1D smoothing operators, one in each grid direction. The parameter e_4 is a user-defined constant, which is kept within the range $0.05 \leqslant e_4 \leqslant 0.10$ during the calculations.

The right-hand side of equations (8) and (9) are calculated in standard manner, i.e. by using the average of cell-centred values for the two cells that share the wall multiplied by the corresponding metric terms. The pressure gradient on the left-hand side of equation (9) can be evaluated in the same manner as the viscous terms in the momentum equations. For example, the integrated flux

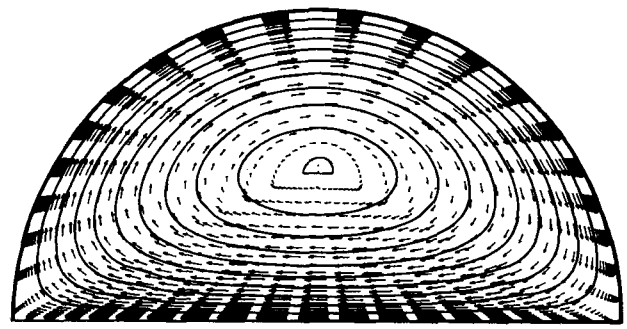

Figure 4. Predicted velocity vector field at the upper surface at $t = 0{\cdot}12T$ compared with the streamline pattern[8] according to potential theory. A velocity vector having magnitude ΩR has a length of $0{\cdot}114R$, and $T = 2\pi/\Omega = 8{\cdot}3s$ is the rotation period

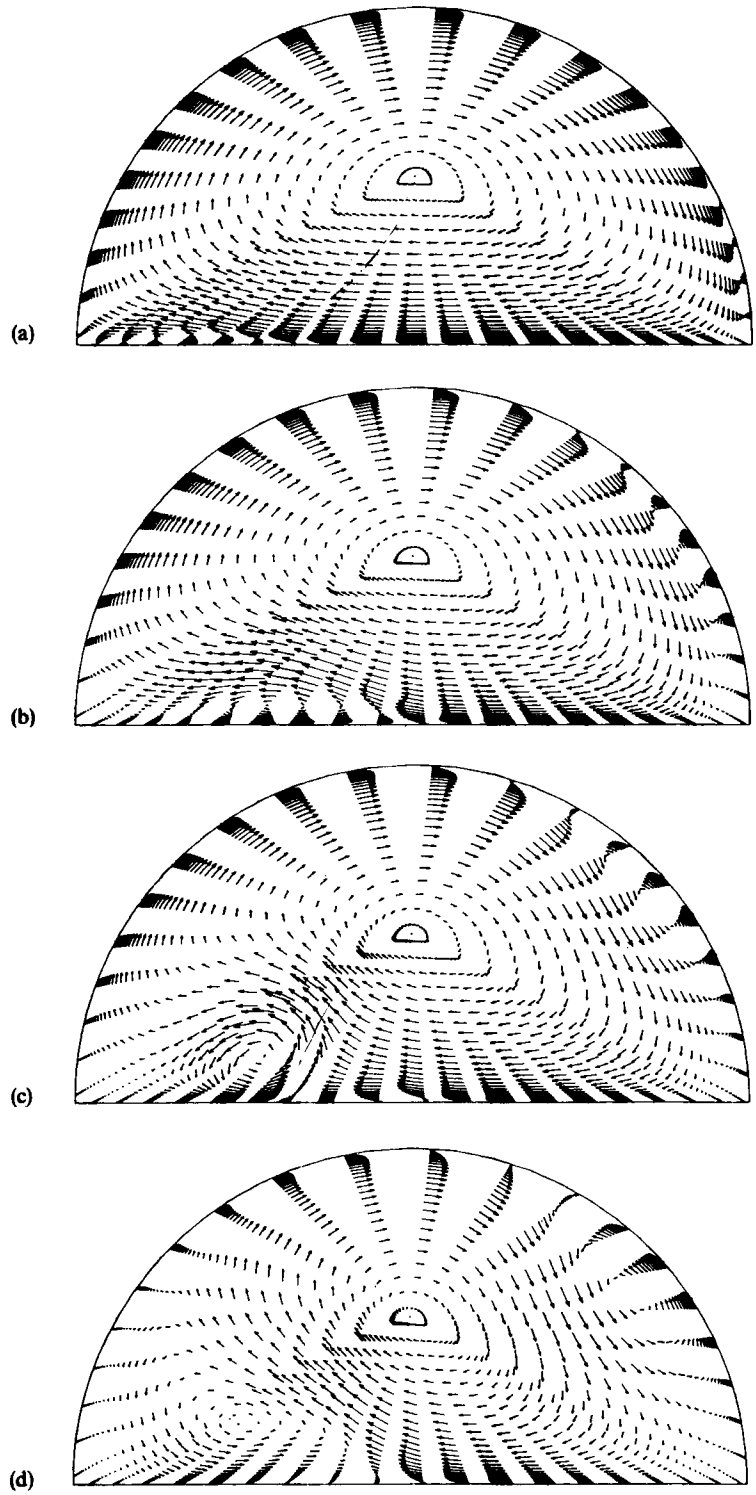

Figure 5. (Continued)

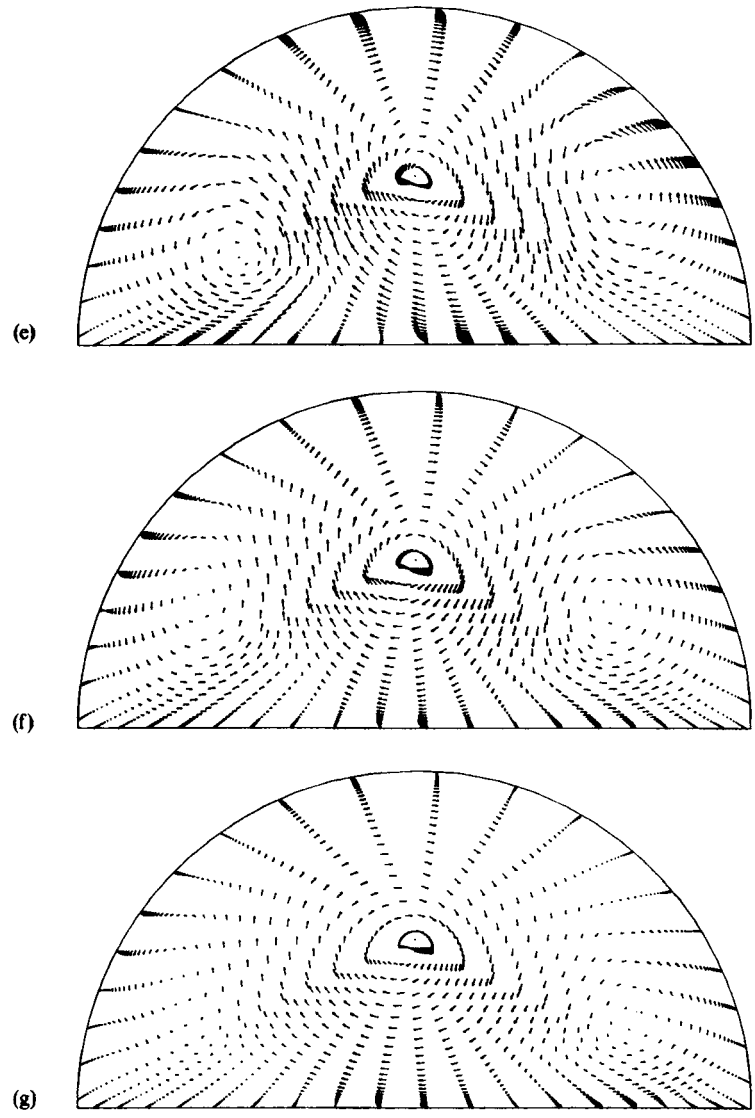

Figure 5. A sequence of velocity vector plots illustrating the predicted evolution of the free-surface flow: (a) $t=0{\cdot}4T$; (b) $t=0{\cdot}7T$; (c) $t=1{\cdot}0T$; (d) $t=1{\cdot}3T$; (e) $t=1{\cdot}8T$; (f) $t=2{\cdot}4T$; (g) $t=3{\cdot}6T$. The scale of the velocity vectors is the same as in Figure 4.

of p/ρ at cell wall $i+1/2, j, k$ can be approximated by

$$[\nabla(p/\rho)\cdot\mathbf{SI}]_{i+1/2,j,k}=\{\mathbf{VOL}^{-1}[|SI|^2\,\partial(p/\rho)/\partial i+\mathbf{SI}\cdot\mathbf{SJ}\,\partial(p/\rho)/\partial j+\mathbf{SI}\cdot\mathbf{SK}\,\partial(p/\rho)/\partial k]\}_{i+1/2,j,k}. \tag{22}$$

Analogous formulas can be written for the corresponding fluxes in the j- and k-directions.

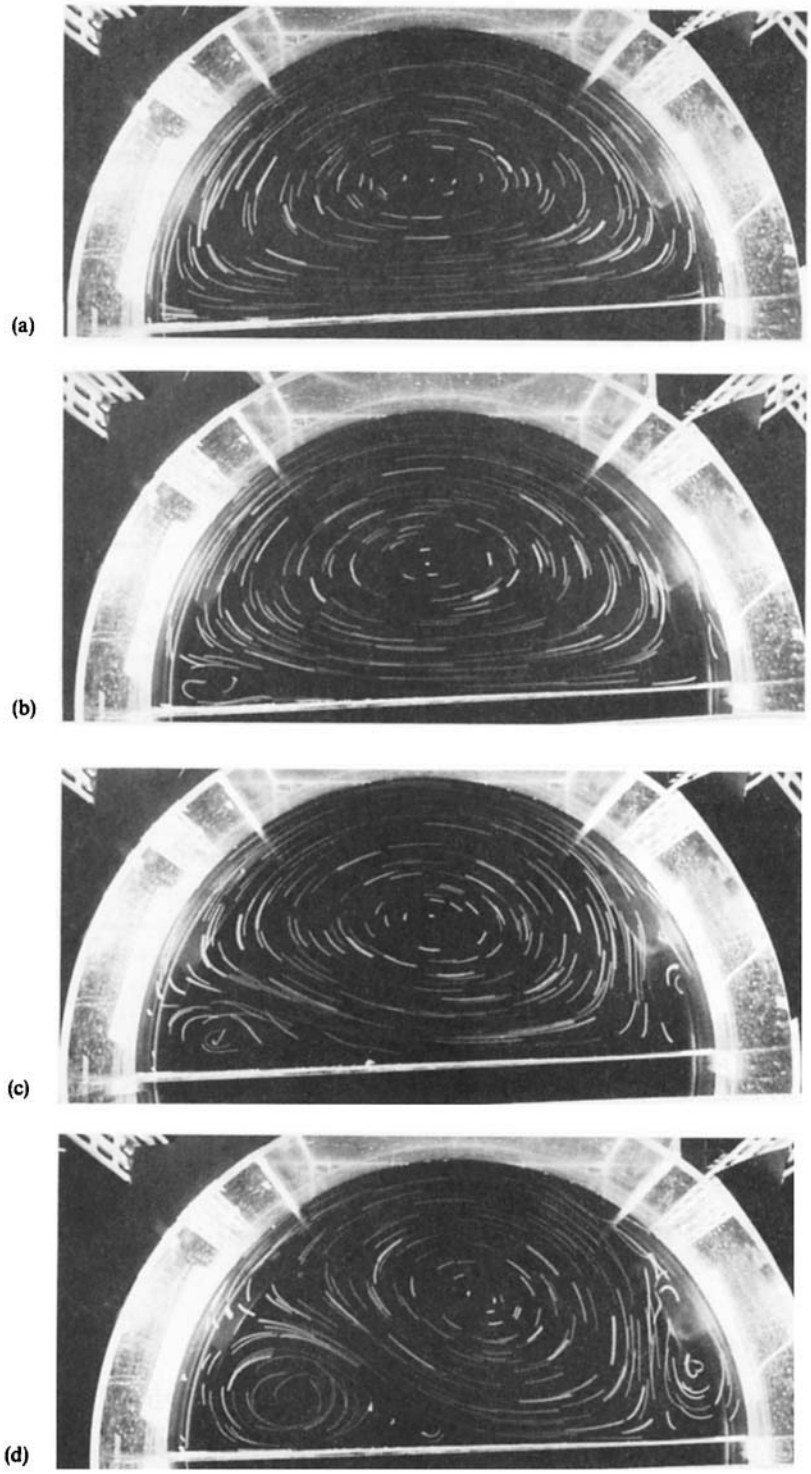

Figure 6. (Continued)

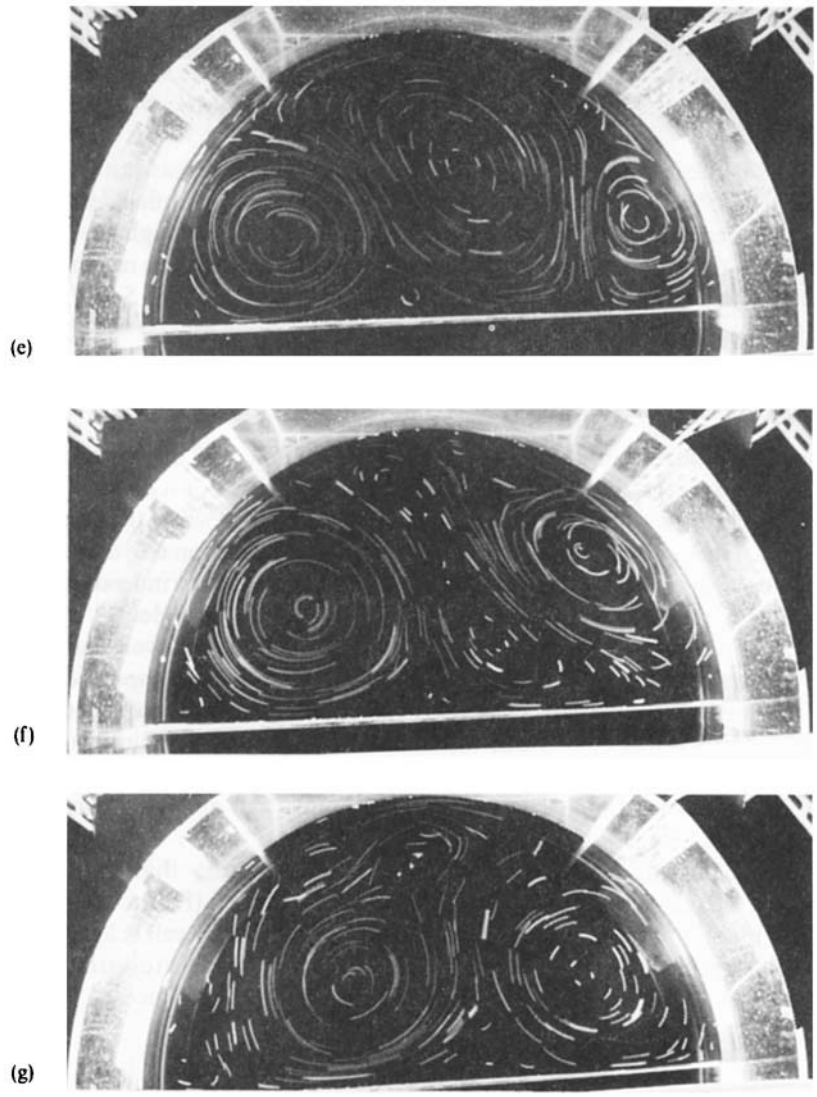

Figure 6. A sequence of streakline photographs showing the evolution of the relative free-surface flow observed in the laboratory: (a) $t = 0{\cdot}4T$; (b) $t = 0{\cdot}7T$; (c) $t = 1{\cdot}0T$; (d) $t = 1{\cdot}3T$; (e) $t = 1{\cdot}8T$; (f) $t = 2{\cdot}4T$; (g) $t = 3{\cdot}6T$. Exposure time 1 s. Here, (a), (c), (e) and (f) have been reproduced from Reference 8 with permission from Cambridge University Press

3.6. Computational details

To facilitate direct comparisons between calculations and experiments, the numerical simulation is carried out with flow parameters identical to those in the experiment reported by van Heijst[8] (see the Figures 10–12 in that paper), i.e. with $H = 12{\cdot}5$ cm, $R = 46{\cdot}2$ cm, $\Omega = 0{\cdot}756$ rad s^{-1}, and $\nu = 1{\cdot}0 \times 10^{-6}$ m^2 s^{-1}. For this particular case the Reynolds number based on the wall velocity ΩR and the Ekman number are $Re = \Omega R^2/\nu = 1{\cdot}6 \times 10^5$ and $E = \nu/\Omega H^2 = 8{\cdot}5 \times 10^{-5}$, respectively.

The grid system used in the calculation consisted of 79 (azimuthal) $\times$ 30 (radial) $\times$ 23 (vertical) points. To obtain a refined mesh in the vicinity of the solid boundaries, i.e. along the vertical side

walls and the horizontal bottom, the grid points were non-uniformly distributed in the radial and vertical directions (see Figure 3). A preliminary simulation with only 16 points in the vertical direction failed to capture the characteristic velocity overshoot in the bottom Ekman layer, while the refined grid with 23 vertical points accurately resolved the velocity gradients of the crucial bottom layer.

At each time level the iterative solver for the Poisson equation (9) was run until the global error became less than 10^{-5} m^3 s^{-2}. To assure stable evolution of the flow field, extremely small time steps Δt were required during the first stages of the simulation. Although the time step could be gradually increased throughout, a total number of some 30 000 steps was required for the solution reported herein. The computer time for the total simulation was about 5 h of CPU-time on the CRAY X-MP 216.

4. COMPARISON OF NUMERICAL AND EXPERIMENTAL RESULTS

The evolution of the flow field at the free surface, as obtained in the numerical simulation, is shown by the velocity vector plots presented in Figures 4 and 5. For a convenient comparison, a sequence of streakline pictures—taken at times corresponding with the numerical results in Figure 5—is shown in Figure 6. It is clear that the computed solution corresponds very well with the laboratory observations. The starting flow (Figures 4 and 6(a)) has indeed the shape of a single anticyclonic cell, for which the streamlines were calculated by van Heijst[8] by use of potential theory. Also, the separation at the downstream ends of both the flat wall and the circular tank wall, as observed in the experiment (Figures 6(b) and 6(c)), is very well captured by the numerical calculation (Figures 5(a)–5(c)). The time scales of the numerical and experimental results do not match exactly, but this is most likely due to the fact that it takes some time in the experiment (a few seconds, typically) to bring the table rotation speed from 0 to Ω. The subsequent growth of the cyclonic cells in the corners of the flow domain (Figures 5(d) and 5(e)) corresponds with the observed flow pattern (Figures 6(d) and 6(e)).

However, for progressing time it is observed in the laboratory that the cyclonic cells shift toward the centre, thereby squeezing the original anticyclonic cell (Figure 6(f)), which ultimately disappears; after merging of the cyclonic cells, only a single cyclonic cell is left in the centre of the flow domain (see Reference 8, Figure 10(e)). This shift of cyclonic cells toward the rotation axis is ascribed to the topographic effect of the curved upper surface (References 8, 9 and 24), and it is

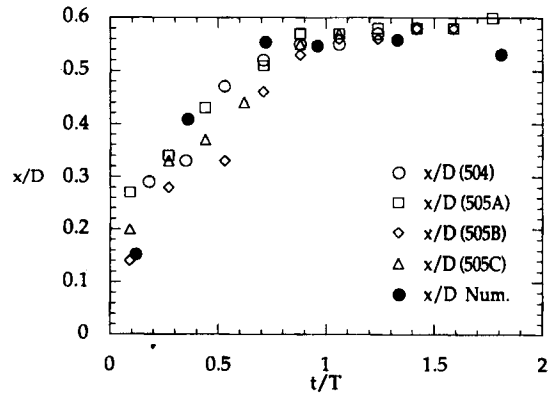

Figure 7. The time-dependent position of the separation point at the flat wall as observed in four laboratory experiments and according to the numerical simulation (see inset for meaning of the symbols). The position x, measured from the downstream end of the flat wall, is non-dimensionalized by $D = 2R$, whereas time t is scaled by the rotation period T

expected that the behaviour of the cyclonic vortices would have been different if the experiment were performed with a rigid lid on top of the fluid. The boundary conditions (4) imposed on the upper surface in the numerical calculation correspond with a rigid lid (with zero shear stress) rather than a free surface, and the different behaviour of the cyclonic cells in the computed flow field confirms the expected role of the free surface.

A characteristic feature of the evolution of the flow field in Figures 5 and 6 is the shifting position of the separation point at the flat wall. Experimentally it is not easy to determine such a moving separation point very accurately, but nevertheless it was attempted by observing (from subsequent photographs) the orientations of some 25 thin flexible yarn threads fixed at regular distances along the downstream half of the flat wall, close to the free surface. Results obtained in four (repeated) experiments are shown in Figure 7, together with a set of data obtained in the numerical simulation: the scaled position x/D of the stagnation point, measured from the downstream end of the flat wall, is plotted versus the non-dimensional time t/T, with T the rotation period of the tank. Although there is some scatter (which is mainly due to the experimental inaccuracy), the data points appear to lie in a well-defined band, indicating a good correspondence between experiments and simulation.

The numerical calculations are essentially 3D; it is, therefore, possible to check to what extent the motion in the bulk region (outside the viscous boundary layers) is 2D. The evolution of the secondary flow pattern in the (r, z)-plane at $\theta = \pi/2$ is illustrated by the plots in Figure 8. In the

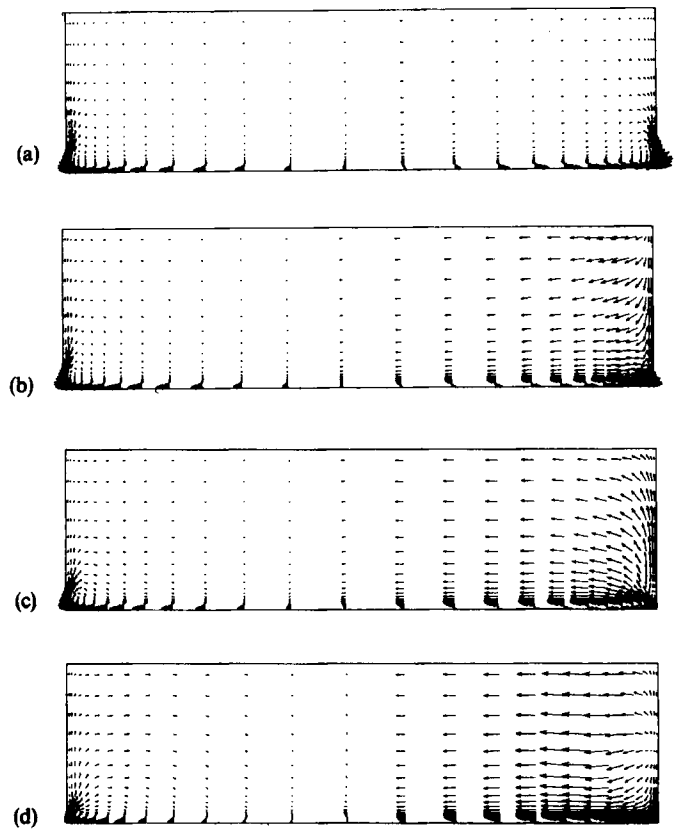

Figure 8. (Continued)

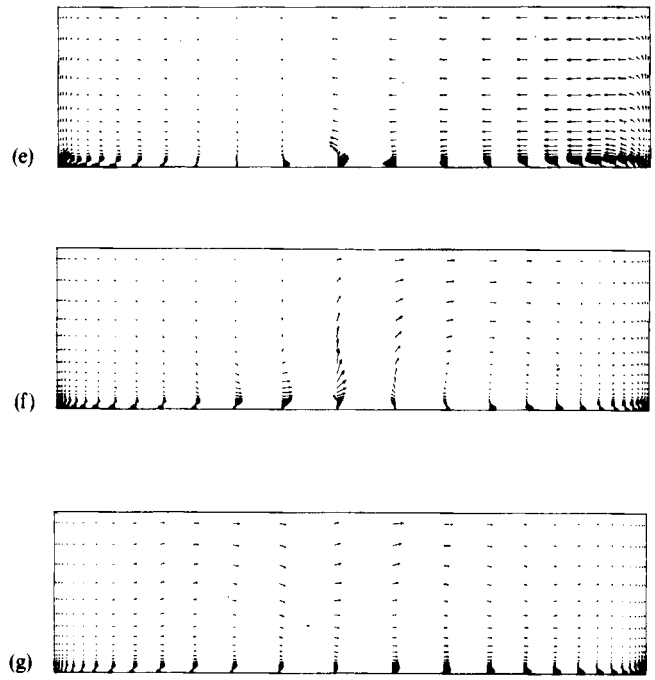

Figure 8. A sequence of velocity vector plots showing the predicted evolution of the secondary circulation in the (vertical) (r, z)-plane at $\theta = \pi/2$. The curved boundary ($r = R$) is on the left, and the flat wall on the right of the pictures: (a) $t = 0{\cdot}4T$; (b) $t = 0{\cdot}7T$; (c) $t = 1{\cdot}0T$; (d) $t = 1{\cdot}3T$; (e) $t = 1{\cdot}8T$; (f) $t = 2{\cdot}4T$; (g) $t = 3{\cdot}6T$. A velocity vector having magnitude ΩR has a length of 0·228R

initial stages (Figure 8(a)–8(e)) a weak radial flow in the bulk region is observed from the curved boundary into the interior region, whereas a more intense 2D radial inflow into the interior takes place at the flat boundary. The vector graphs clearly demonstrate the importance of the bottom Ekman layers, in which the flow is directed radially outwards from the centre of the semi-circular region, as well as that of the side-wall Stewartson layers, which carry axial transports that balance the radial Ekman-layer transports. A somewhat odd reversal of the axial momentum transport along the flat wall is observed at $t = 0{\cdot}7\,T$ in Figure 8(b). This phenomenon is obviously associated with the passage of the separation point (see Figure 5(b)), which in turn implies rapidly changing velocity gradients in the horizontal plane. The resulting excessive horizontal mass flux into the computational cell next to $r = 0$ at the free surface can only be compensated by a fairly strong downward motion at the flat wall.

Another flow reversal is taking place in the Ekman layer in the vicinity of the centre of the horizontal bottom, i.e. near $r = R/2$, at $t = 1{\cdot}8T$ (Figure 8(e)). The reversal of the Ekman layer transport is followed by a sudden change in the entire secondary circulation pattern (see Figure 8(f)). This event takes place when the centre of the original anticyclonic cell (being pushed by the gradually increasing cyclonic cell at the curved wall) passes the vertical symmetry plane, thereby changing the direction of the radial velocity component. Then, at $t = 3{\cdot}6\,T$, a weak and wavy flow is directed radially from the curved wall towards the plane wall (Figure 8(g)).

The presence of the bottom Ekman layer can also be clearly observed in the vertical distribution of the azimuthal velocity in the vertical (r, z)-plane at $\theta = \pi/2$, see Figure 9. According

to the velocity profiles, the thickness of the bottom layer is approximately 0.5 cm, which corresponds with the theoretical estimate $\delta \approx LRe^{-1/2}$, with L a typical horizontal scale and Re the Reynolds number based on L. Also, the profiles clearly exhibit the characteristic velocity overshoot, which is only resolved with the highly non-uniform grid distribution in vertical direction (see Figure 3(b)). When a somewhat coarser grid is used (16 instead of 23 vertical grid volumes), the overshoot peaks are not captured.

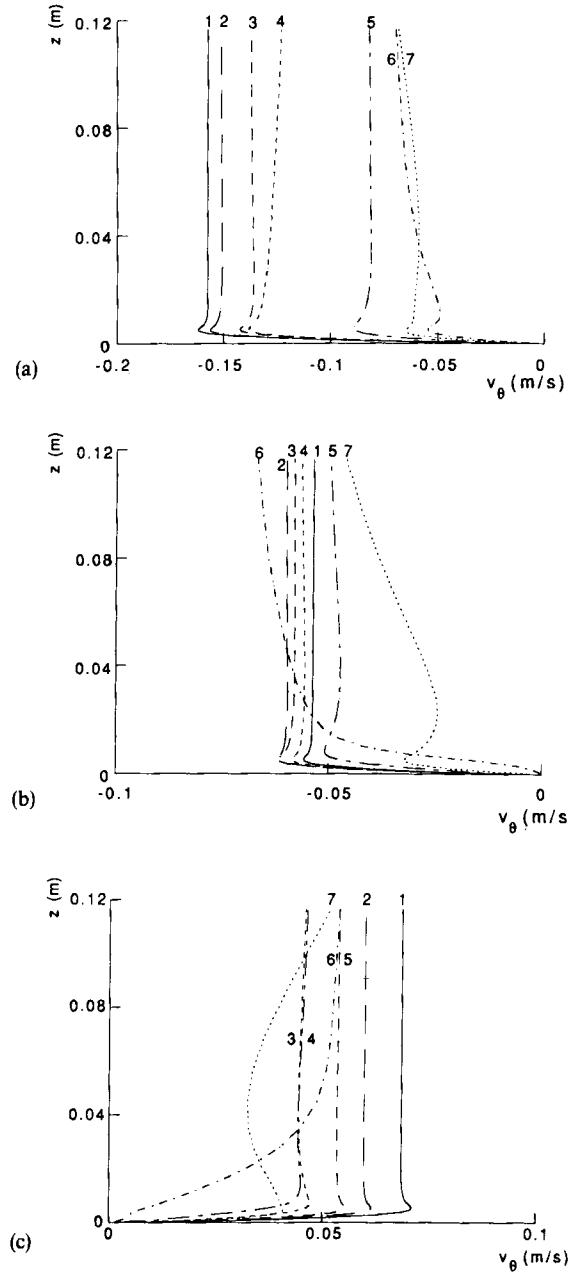

Figure 9. (Continued)

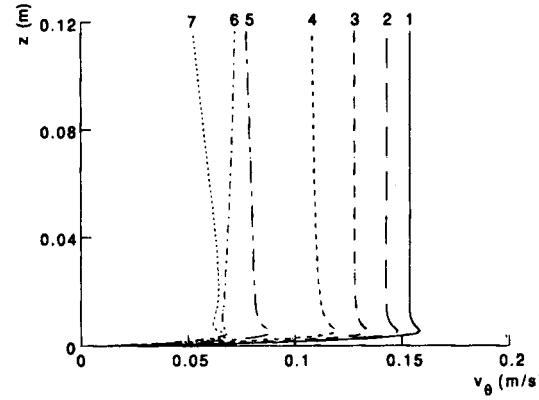

Figure 9. Graphs showing the calculated evolution with time of the vertical distribution of the azimuthal velocity component v_θ in the vertical midplane ($\theta=\pi/2$) for different radial positions: (a) $r=0{\cdot}2R$; (b) $r=0{\cdot}4R$; (c) $r=0{\cdot}6R$; (d) $r=0{\cdot}8R$. The times correspond with those of Figure 5

It is clearly seen from the velocity profiles that the flow outside the bottom layer is (in most stages of the adjustment process) essentially 2D, confirming the assumption that the free-surface flow is indeed representative of the flow at lower levels. The velocity profiles show gradual changes during the spin-up process due to changes in the horizontal flow pattern (see Figure 5), while the thickness of the Ekman layer remains approximately constant. At about $t=2{\cdot}4T$, however, a dramatic change in the vertical distribution of the azimuthal velocity takes place near the centre of the flow domain, in particular at $r=0{\cdot}4R$ and $0{\cdot}6R$ (see Figures 9(b) and 9(c)). This change is associated with a local breakdown of the Ekman layers, and corresponds with an intense upwash of fluid in the centre of the flow domain ($r=0{\cdot}5R$) at this particular instant (see also Figure 8(f)). Then, at $t=3{\cdot}6T$, the Ekman layer has been reestablished (see Figures 9(b) and 9(c)), although the flow in the central area is still not z-independent at that stage. When the simulation was carried on for another $0{\cdot}36T$, a reestablishment of the two-dimensionality of the bulk flow was observed, while the internal waviness decayed.

Important information about the predicted flow behaviour in the first stages of the spin-up process is provided by the isovorticity contour plots displayed in Figure 10. The sequence of plots clearly shows that in the initial stage the predicted vorticity in the interior has indeed a uniform value (as was assumed in the analytical approach to this flow, see van Heijst[8]), and that narrow regions of large positive vorticity occur along the sidewalls of the flow domain (Figure 10(a)). The occurrence of these regions is directly associated with the viscous boundary layers in which positive vorticity is generated. In the next stage, see Figure 10(b), these regions are observed to grow in size; comparison with the corresponding velocity vector plot (Figure 5(b)) reveals that flow separation has started at this stage, and that return flows occur in those regions with positive vorticity. In the next few stages it is seen how the positive vorticity areas become larger, and gradually move away from the boundaries (Figures 10(c)–10(e)): their positions coincide with those of the cyclonic cells visible in Figure 5.

An important point worth noting is the changing distribution of negative vorticity in the flow domain. Initially, the negative vorticity was almost uniformly distributed over the area, with some regions of larger gradients adjacent to the viscous shear layers (see Figure 10(a)). The sequence of vorticity contour plots clearly shows the eventual formation of a single cell of negative vorticity in the centre, with some narrow regions of negative vorticity against the flow boundaries, as a

consequence of the boundary layers due to the cyclonic cells (Figure 10(f)). Once this cellular pattern is established, the vorticity shows a remarkably *smooth* distribution over both the positive and the negative vorticity cells: although initially large gradients and high-vorticity values occur in the viscosity-dominated regions (Figure 10(a)), once the cells have separated from the walls the gradients become gradually weaker, while the extreme values are seen to decrease (Figure 10(f)).

The vorticity contour plots thus clearly demonstrate the crucial role the boundary layers at the sidewalls of the container play during the first stages of the spin-up process: they are responsible

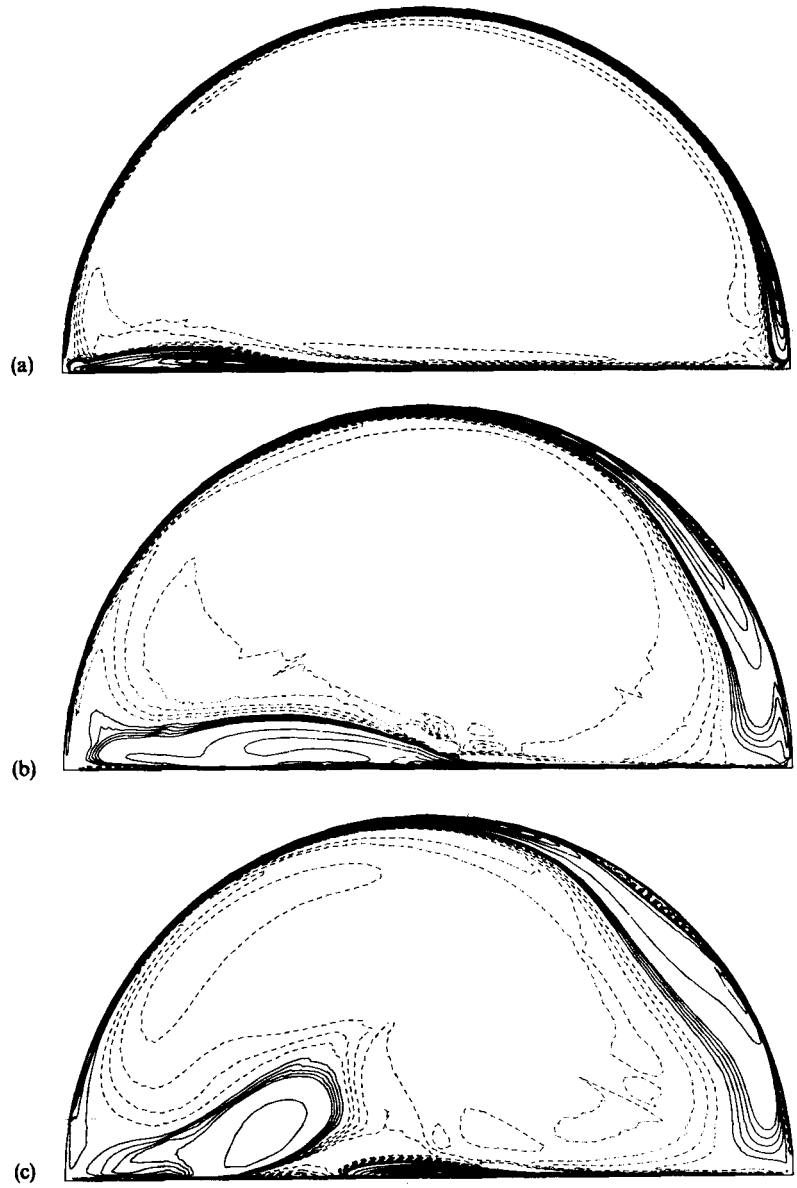

Figure 10. (Continued)

(d)

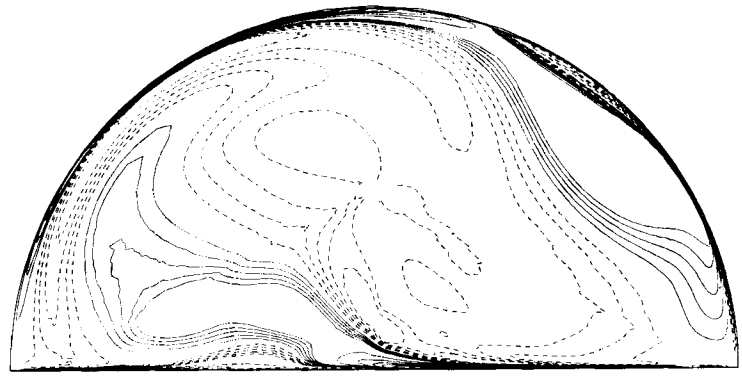

(e)

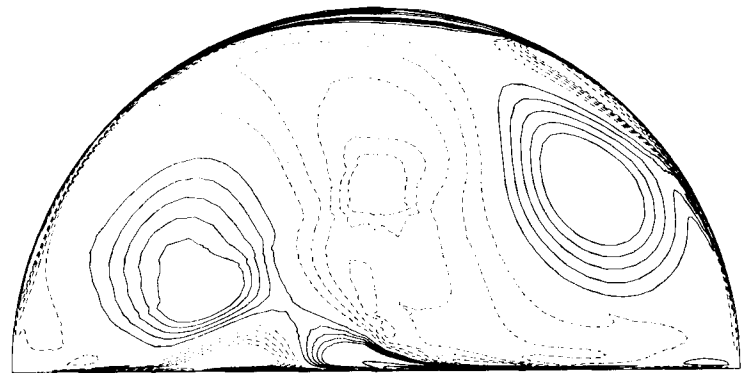

(f)

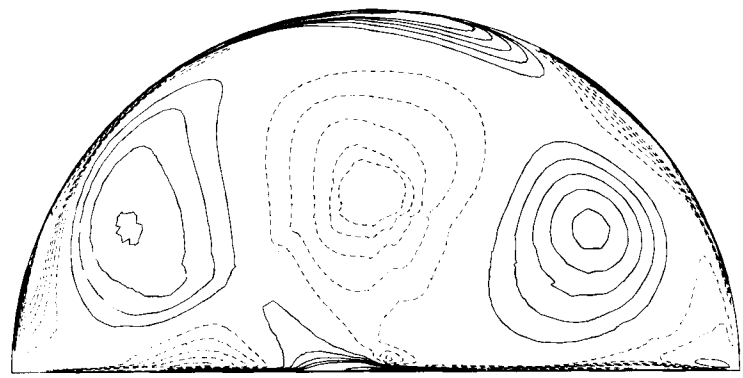

Figure 10. (Continued)

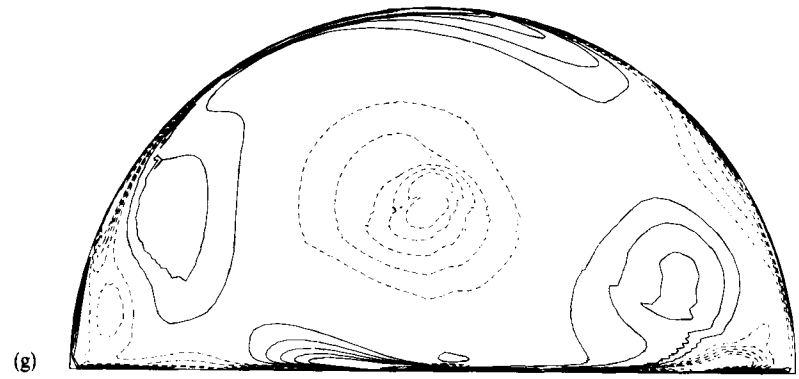

Figure 10. A sequence of isovorticity plots corresponding with the sequence shown in Figure 5. The contours represent the predicted vertical component ω_z of the vorticity at the free surface. Contours are plotted for the range $-1{\cdot}0 \leqslant \omega_z \leqslant 1{\cdot}0$ with $\Delta\omega_z = 0{\cdot}2\ s^{-1}$ and with $\Delta\omega_z = 2{\cdot}0\ s^{-1}$ outside this range. Regions of positive and negative vorticity are indicated by solid and broken lines, respectively: (a) $t = 0{\cdot}4T$; (b) $t = 0{\cdot}7T$ (c) $t = 1{\cdot}0T$, (d) $t = 1{\cdot}3T$; (e) $t = 1{\cdot}8T$; (f) $t = 2{\cdot}4T$; (g) $t = 3{\cdot}6T$

for the viscous *production* as well as the *advection* of cyclonic vorticity, which leads to the generation of the cyclonic flow cells. One thus obtains clearly recognizable regions of positive and negative vorticity, which tend to grow (owing to the 2D nature of the flow) until they reach the physical boundaries (sidewalls), after which they fill the entire flow domain according to some regular cellular pattern. It is in this quasi-ultimate stage that the bottom Ekman layer comes seriously into play: it drives a secondary circulation within each individual cell, which results in the spin-up or spin-down of the cells similar to the flow in an axisymmetric container as considered by Greenspan and Howard.[2] Because the formation of the cellular pattern is already established within a few revolutions of the system, the total spin-up time (i.e. the time required for the fluid to reach the final state of solid-body rotation with angular velocity Ω) is effectively equal to the classical Ekman timescale $T_E = H/(\nu\Omega)^{1/2}$.

5. CONCLUDING REMARKS

The primary purpose of the present work was to simulate the 3D spin-up flow in a semicircular container by solving the time-dependent Navier–Stokes equations for incompressible fluid motion. Computed results were compared with laboratory observations and essentially good agreement was obtained during the first stages of the spin-up process. It can, therefore, be concluded that the Navier–Stokes equations (without any turbulence model) realistically model the start-up flow, and that the present numerical scheme is capable of solving this mathematical model with an acceptable degree of accuracy.

Moreover, the numerically simulated flow field revealed some important information about the 3D flow phenomena:

(i) The bulk flow (outside the viscous boundary layers) is essentially 2D.
(ii) The thickness of the Ekman layer remains approximately constant during the simulation.
(iii) An unexpected reversal of the secondary circulation pattern takes place when the anti-cyclonic cell shifts its position.

In the latest stage of the simulation the organization of the cell pattern became essentially different from the laboratory flow. While the observed shift of the cyclonic cells towards the centre

of the domain has been ascribed to the presence of the free surface,[9] the inviscid rigid-lid upper boundary condition (4) is responsible for the survival of the central anticyclonic cell in the simulated flow field. To capture the observed effect of the free surface in a numerical simulation, a mathematical model which accounts for the mass defect due to free-surface depressions associated with the cyclonic vortices is needed.

REFERENCES

1. E. R. Benton and A. Clark, 'Spin-up', *Ann. Rev. Fluid Mech.*, **6**, 257–280 (1974).
2. H. P. Greenspan and L. N. Howard, 'On a time-dependent motion of a rotating fluid', *J. Fluid Mech.*, **17**, 385–404 (1963).
3. J. R. Holton, 'The influence of viscous boundary layers on transient motions in a stratified rotating fluid. Part 1', *J. Atmos. Sci.*, **22**, 402–411 (1965).
4. J. Pedlosky, 'The spin-up of a stratified fluid', *J. Fluid Mech.*, **28**, 463–480 (1967).
5. G. Walin, 'Some aspects of time-dependent motion of a stratified rotating fluid', *J. Fluid Mech.*, **36**, 289–307 (1969).
6. G. Buzyna and G. Veronis, 'Spin-up of a stratified fluid: theory and experiment', *J. Fluid Mech.*, **50**, 579–608 (1971).
7. P. F. Linden and G. J. F. van Heijst, 'Two-layer spin-up and frontogenesis', *J. Fluid Mech.*, **143**, 69–94 (1984).
8. G. J. F. van Heijst, 'Spin-up phenomena in non-axisymmetric containers', *J. Fluid Mech.*, **206**, 171–191 (1989).
9. G. J. F. van Heijst, P. A. Davies and R. G. Davis, 'Spin-up in rectangular containers', *Phys. Fluids*, **A2**, 150–159 (1990).
10. J. T. Billdal and H. I. Andersson, 'A finite-volume method for time-dependent Navier–Stokes equations in rotating systems', *Proc. 7th Int. Conf. on Numerical Methods in Laminar and Turbulent Flow*, Pineridge Press, Swansea, 1991, pp. 443–453.
11. A. K. Rastogi and W. Rodi, 'Predictions of heat and mass transfer in open channels', *ASCE J. Hydraulics Div.*, **104**, 397–420 (1978).
12. M. A. Leschziner and W. Rodi, 'Calculation of strongly curved open channel flow', *ASCE J. Hydraulics Div.*, **105**, 1297–1314 (1979).
13. A. J. Chorin, 'A numerical method for solving incompressible viscous flow problems', *J. Comput. Phys.*, **2**, 12–26 (1967).
14. J. T. Billdal, Ø. Jacobsen, K. Bratsberg, H. I. Andersson and H. Brekke, 'Numerical inviscid flow analysis of the GAMM Francis runner', *3D Computation of Incompressible Internal Flows, Notes on Numerical Fluid Mechanics*, Vieweg Verlag, 1992 (in press).
15. R. Kristoffersen, J. T. Billdal and H. I. Andersson, 'The three-dimensional lid-driven cavity flow as test case for numerical solution algorithms, *Proc. 6th Int. Conf. on Numerical Methods in Laminar and Turbulent Flow*, Pineridge Press, Swansea, 1989, pp. 133–143.
16. Ø. Jacobsen, H. I. Andersson, J. T. Billdal and H. Brekke, 'Three-dimensional turbulent flow simulation in hydraulic machinery', *Proc. 15th IAHR Symposium on Modern Technology in Hydraulic Energy Production, Vol 1*, 1990, paper C3.
17. A. J. Chorin, 'Numerical solutions of the Navier–Stokes equations', *Math. Comput.*, **22**, 745–762 (1968).
18. R. Témam, 'Sur l'approximation de la solution des équations de Navier–Stokes par la méthode des pas fractionnaires (II)',*Arch. Rat. Mech. Anal.*, **32**, 377–385 (1969).
19. M. Fortin, R. Peyret and R. Témam, 'Résolution numérique des équations de Navier–Stokes pour un fluide incompressible', *J. Méc.*, **10**, 357–390 (1971).
20. R. Peyret and T. D. Taylor, *Computational Methods for Fluid Flow*, Springer, New York, 1983.
21. H. I. Andersson, J. T. Billdal, P. Eliasson and A. Rizzi, 'Staggered and non-staggered finite-volume methods for nonsteady viscous flows: a comparative study', *Proc. 12th Int. Conf. on Numerical Methods in Fluid Dynamics, Lecture Notes in Physics* 371, Springer, 1990, pp. 172–176.
22. A. Rizzi and L.-E. Eriksson, 'Computation of flow around wings based on the Euler equations', *J. Fluid Mech.*, **148**, 45–71 (1984).
23. L.-E. Eriksson, A. Rizzi and J. P. Therre, 'Numerical solutions of the steady incompressible Euler equations applied to water turbines', *AIAA 2nd Applied Aerodynamics Conference*, AIAA Paper 84–2145 (1984).
24. G. F. Carnevale, R. C. Kloosterziel and G. J. F. van Heijst, 'Propagation of barotropic vortices over topography in a rotating tank', *J. Fluid Mech.*, **233**, 119–139 (1991).